# Geodynamic Modeling with Uncertain Initial Geometries

Arne Spang[1,1], Tobias Baumann[1,1], and Boris J.P. Kaus[1,1]

[1]Johannes Gutenberg University

November 30, 2022

**Abstract**

Geodynamic codes have become fast and efficient enough to facilitate sensitivity analysis of rheological parameters. With sufficient data, they can even be inverted for. Yet, the geodynamic inverse problem is often regularized by assuming a constant geometry of the geological setting (e.g. shape, location and size of salt diapirs or magma bodies) or approximating irregular bodies with simple shapes like boxes, spheres or ellipsoids to reduce the parameter space. Here, we present a simple and intuitive method to parameterize complex 3D bodies and incorporate them into geodynamic inverse problems. The approach can automatically create an entire ensemble of initial geometries, enabling us to account for uncertainties in imaging data. Furthermore, it allows us to investigate the sensitivity of the model results to geometrical properties and facilitates inverting for them. We demonstrate the method with two examples. A salt diapir in an extending regime and free subduction of an oceanic plate under a continent. In both cases, small differences in the model's initial geometry lead to vastly different results. Be it the formation of faults or the velocity of plates. Using the salt diapir example, we demonstrate that, given an additional geophysical observation, we are able to invert for uncertain geometric properties. This highlights that geodynamic studies should investigate the sensitivity of their models to the initial geometry and include it in their inversion framework. We make our method available as part of the open-source software geomIO.

# Geodynamic Modeling with Uncertain Initial Geometries

**A. Spang [1], T. S. Baumann [1], B. J. P. Kaus [1,2]**

[1]Johannes Gutenberg University, Institute of Geosciences, Johann-Joachim-Becher-Weg 21, 55128 Mainz, Germany

[2]TeMaS, Terrestrial Magmatic Systems Research Center, temas.uni-mainz.de

**Key Points:**

- New, simple, intuitive and open-source method to describe and manipulate complex 3D bodies with a small number of parameters
- Allows for the integration of uncertainties of the initial geometry and enables inverting for geometric properties in numerical models
- Applications to a salt diapir with uncertain initial geometry and a subduction zone with uncertain initial subduction angle

Corresponding author: Arne Spang, `arspang@uni-mainz.de`



This article has been accepted for publication and undergone full peer review but has not been through the copyediting, typesetting, pagination and proofreading process, which may lead to differences between this version and the Version of Record. Please cite this article as doi: 10.1029/2021GC010265.

## Abstract

Geodynamic codes have become fast and efficient enough to facilitate sensitivity analysis of rheological parameters. With sufficient data, they can even be inverted for. Yet, the geodynamic inverse problem is often regularized by assuming a constant geometry of the geological setting (e.g. shape, location and size of salt diapirs or magma bodies) or approximating irregular bodies with simple shapes like boxes, spheres or ellipsoids to reduce the parameter space. Here, we present a simple and intuitive method to parameterize complex 3D bodies and incorporate them into geodynamic inverse problems. The approach can automatically create an entire ensemble of initial geometries, enabling us to account for uncertainties in imaging data. Furthermore, it allows us to investigate the sensitivity of the model results to geometrical properties and facilitates inverting for them. We demonstrate the method with two examples. A salt diapir in an extending regime and free subduction of an oceanic plate under a continent. In both cases, small differences in the model's initial geometry lead to vastly different results. Be it the formation of faults or the velocity of plates. Using the salt diapir example, we demonstrate that, given an additional geophysical observation, we are able to invert for uncertain geometric properties. This highlights that geodynamic studies should investigate the sensitivity of their models to the initial geometry and include it in their inversion framework. We make our method available as part of the open-source software geomIO.


## Plain Language Summary

Computer models of geological settings have become a popular tool of research. They require the user to provide information on where the different geological units (rock layers, salt domes, magma bodies etc.) start and end as well as material parameters like density and strength of the units. As many of these input parameters are not well known, a lot of studies perform multiple simulations with different parameter combinations to investigate the influence the individual parameters and their uncertainties have. However, the initial geometry often remains fixed as it is difficult to describe with only few parameters and therefore unrealistic to vary. Here, we present a new method to describe and manipulate the geometry of geological units with a small number of parameters. This allows us to also vary the initial geometry and investigate how the model results depend on it. We apply our method to a salt diapir and a subduction zone to demonstrate the impact of initial geometry on the simulation results. To make our method available to the community, we implement it as a tool into geomIO, an open-source software package to generate initial geometries for geodynamic models.

## Index Terms

1976 Software tools and services
0545 Modeling
8118 Dynamics and mechanics of faulting
8170 Subduction zone processes
3275 Uncertainty quantification

## Keywords

Geometry Parameterization, Variable Geometry, Salt Tectonics, Subduction Velocity, Inversion, Subduction Angle

## 1 Introduction

Geodynamic modeling has become a powerful tool to investigate how different mechanical and thermodynamical parameters influence and control geological systems such as orogens, subduction zones, magmatic systems, basins and other terrestrial bodies (e.g., Alisic et al., 2010; Jadamec et al., 2013; Baumann & Kaus, 2015; Ratnaswamy et al., 2015; Reuber et al., 2018). With the help of observations, the abovementioned studies can constrain rheology, density and thermal properties of geological units with forward and inverse approaches.

It is common practice in geodynamic modeling to assign material properties such as density and rheology in space with the help of geometrical objects that approximate units like rock layers, magma bodies or tectonic plates (van Zelst et al., 2021). There is a collection of open-source software packages covering this task. UWGeodynamics (Beucher et al., 2019, https://uwgeodynamics.readthedocs.io/) uses simple geometrical objects and polyhedra to generate setups for the Underworld code (Moresi et al., 2002, https://www.underworldcode.org/). GemPy (e.g. Varga et al., 2019; Schaaf et al., 2021, https://www.gempy.org/) allows the creation of layered and folded rock units, including faults and shapes like magma bodies and provides tools for gravity modeling and uncertainty analysis. The Geodynamic World Builder

(Fraters et al., 2019, https://geodynamicworldbuilder.github.io/) focuses on ocean settings like subduction zones and spreading centers and is compatible with various geodynamic codes. Tect_Mod3D (formerly SlabGenerator, e.g. Jadamec et al., 2013) is another software geared towards subduction zones. Easy (https://easyinit.readthedocs.io/) provides several tools to set initial conditions. geomIO (Bauville & Baumann, 2019, https://bitbucket.org/geomio/geomio) allows for the creation of 3D setups from vector graphic drawings (in Inkscape), provides gravity forward modeling and is coupled to the thermomechanical code LaMEM (Kaus et al., 2016).

Unlike the material properties themselves, the initial geometry of geodynamic models is usually treated as a constant throughout the study and not included in any parameter variations. This is because creating the initial geometry is, especially in three dimensions (3D), a time consuming process and parameterization is difficult (van Zelst et al., 2021). While the density of a geological unit can be described with a single number, defining its location and boundaries involves a large number of parameters if its shape is more complex than a basic geometric bodies such as planes, boxes, spheres or ellipsoids. Because of that, many modeling studies (e.g, Pearse & Fialko, 2010; Baumann et al., 2014; Čížková & Bina, 2015, and previously mentioned geodynamic studies) do not only have to ignore the uncertainties that are associated with the initial geometry but also lose the ability to investigate the influence of the initial geometry on the model results. Other studies generate different initial geometries and demonstrate a link between geometry and results, but can either not parameterize the geometry (e.g. Le Pourhiet et al., 2003) or are bound to simple properties like the thickness of a horizontal, planar layer (e.g. Duretz et al., 2020).

To facilitate the inclusion of a flexible geometry in geodynamic investigations, it needs to be efficiently parameterized with a number of geometrical parameters that does not outweigh the number of material parameters. Flexible geometries are commonly used in geomodeling (Wellmann & Caumon, 2018), potential-field modeling like gravity and magnetics (Jessell, 2001) and seismic inversion (Bosch et al., 2010). Techniques include voxel models (e.g. Guillen et al., 2004), discrete object modeling (e.g. Oldenburg & Pratt, 2007), flexible prisms (e.g., Fullagar et al., 2000), parameterized surfaces (e.g. Pereyra, 1996), explicit surfaces (e.g. Caumon et al., 2009) and implicit surfaces (e.g. Frank et al., 2007) but most approaches result in a collection of triangulated surfaces and/or voxel models (Galley et al., 2020).

It is our aim to present a method to intuitively parameterize and vary the 3D geometry of key features (e.g. salt domes, magma bodies, subducting slabs) of geodynamic models. The method is implemented as a tool in geomIO (https://bitbucket.org/geomio/geomio) including a user manual and examples (https://bitbucket.org/geomio/geomio/wiki/VaryGeomTutorial.md) and is fully coupled to a state-of-the-art thermomechanical code in LaMEM (https://bitbucket.org/bkaus/lamem/src/master/). This facilitates the inclusion of geometric uncertainties in geodynamic modeling and enables us to constrain geometric properties of subsurface geological features with surface observations.

In section 2, we present the method and show examples of how it works for arbitrary shapes and subducting plates. In section 3, the method is applied to 2 different geological scenarios. (i) Seismic reflection reveals a salt diapir but its horizontal and vertical extent are uncertain. We generate an ensemble of possible initial geometries and demonstrate that they lead to distinctly different faulting patterns. This allows us to link geometric features to model results and constrain the geometry of the diapir with a synthetic surface observation. (ii) We model free subduction of an oceanic plate underneath a continent and investigate the dependence of the velocities of both plates on the initial dip angle of the subducting slab. We also track the evolution of the dip angle as the plate subducts and compare the results to natural observations.

## 2 Methods

Our method is based on changing a single body at a time. As the definition of any complex 3D shape requires a large number of coordinates, we always need a reference model or starting geometry, which may be any 3D volume that is not a non-manifold geometry. We then create parameters which describe a transformation of this reference model into a different shape. Section 2.1 describes our general transformation algorithm applicable to any shape, and section 2.2 shows an example of how it can be used to transform a sphere into a more complex shape. Section 2.3 shows how the method can be adapted for a subduction setting. Supplementary text S1 and Figure S1 explain the workflow of using the method in a geodynamic study.

## 2.1 Transformation Algorithm

### 2.1.1 *Scaling Parameters*

To manipulate the reference model, we compute the intersection of the 3D body with a finite number of horizontal planes that are perpendicular to the z-direction. In a second step, we select a subset of the resulting two-dimensional (2D) polygons (red in Figure 1a), which are referred to as control polygons. For each of the control polygons ($P_i$) we define two scaling parameters ($Sx_i$ and $Sy_i$) and compute scaling parameters for all other polygons in the following manner:

(i) Polygons below the lowermost control polygon copy its scaling parameters.
(ii) The scaling parameters of polygons between two control polygons are linearly interpolated between those of the control polygons.
(iii) Polygons above the uppermost control polygon copy its scaling parameters.

To achieve a homogeneous transformation in the horizontal plane, $Sx_i$ must equal $Sy_i$ which reduces the number of necessary parameters to one per control polygon. Finally, there is a single parameter ($Sz$) to transform the body in the vertical direction.

### 2.1.2 *Vertical Scaling*

To scale the body in the vertical direction, the spacing between the polygons is multiplied by the vertical scaling parameter ($Sz$):

$$z_{i,new} = (z_i - z_{ref}) * Sz + z_{ref} \tag{1}$$

Where $z_i$ is the vertical coordinate of the polygon and $z_{ref}$ is the reference depth of vertical scaling. If $Sz > 1$, the body is vertically extended, if $Sz < 1$, the body is shrunk. $z_{ref}$ should be chosen in dependence of the object to be transformed. For shapes like magma or ore bodies that are not bound to another unit, it makes sense to use the body's center of mass while for a salt diapir, its base is more appropriate.

#### *2.1.3 Horizontal Scaling*

To scale the body in the two horizontal directions, the following steps are applied to each polygon individually. First, we compute the position of the polygon's center of mass and transform the coordinates of all nodes on the polygon to be relative to it:

$$\begin{pmatrix} \vec{x_i}' & \vec{y_i}' \end{pmatrix} = \begin{pmatrix} \vec{x_i} & \vec{y_i} \end{pmatrix} - \begin{pmatrix} x_{i_c} & y_{i_c} \\ ... & \\ x_{i_c} & y_{i_c} \end{pmatrix} \tag{2}$$

Where $\vec{x_i}'$ and $\vec{y_i}'$ are vectors containing the relative coordinates of the nodes of the polygon, $\vec{x_i}$ and $\vec{y_i}$ are vectors containing the absolute coordinates of the nodes and $x_{i_c}$ and $y_{i_c}$ are the absolute coordinates of the polygon's center of mass. Then, all x-coordinates are multiplied by $Sx_i$ and all y-coordinates by $Sy_i$. Lastly, the coordinates are transformed back into absolute values:

$$\begin{pmatrix} \vec{x}_{i,new} & \vec{y}_{i,new} \end{pmatrix} = \begin{pmatrix} \vec{x_i}' & \vec{y_i}' \end{pmatrix} * \begin{pmatrix} Sx_i & 0 \\ 0 & Sy_i \end{pmatrix} + \begin{pmatrix} x_{i_c} & y_{i_c} \\ ... & \\ x_{i_c} & y_{i_c} \end{pmatrix} \tag{3}$$

If $Sx_i > 1$, the polygon extends in x-direction and if $Sx_i < 1$, the polygon shrinks. The same is true for $Sy_i$ and the y-direction.

#### *2.1.4 Additional Options*

Equations 1 - 3 are the core of our method and sufficient to describe all operations used in the following example and the application in section 3.1. Supplementary text S2 describes additional options that we implemented.

### 2.2 Example

For the sake of convenient visualization, we choose a sphere as our reference model. We represent the sphere with 21 equally spaced, horizontal polygons (Figure 1a) but the number of plain intersections is arbitrary. Polygons 13, 15 and 19 are chosen to be control polygons (red in Figure 1a) and for each one we set the parameters $Sx$ and $Sy$ (red in table 1). The other scaling parameters are then computed according to section 2.1.1

and used to transform the sphere in Figure 1a into the shape shown in Figure 1b. As we did not specify a vertical scaling parameter $Sz$, the body does not change its height. Figure 1c shows another example using the same parameters of table 1 with $Sz = 0.6$.

The procedure can be imagined as pulling ($S > 1$) or pinching ($S < 1$) a rubber object at the locations of the control polygons. The only difference being, that the top and bottom of the object are not fixed but deform together with the closest control polygon. To keep top or bottom fixed, simply make the first (bottom) or last (top) polygon a control polygon with $S = 1$.

The number and position of the control polygons and the scaling parameters can be chosen by the user. Examples of using the tool are given at:
https://bitbucket.org/geomio/geomio/wiki/VaryGeomTutorial.md.

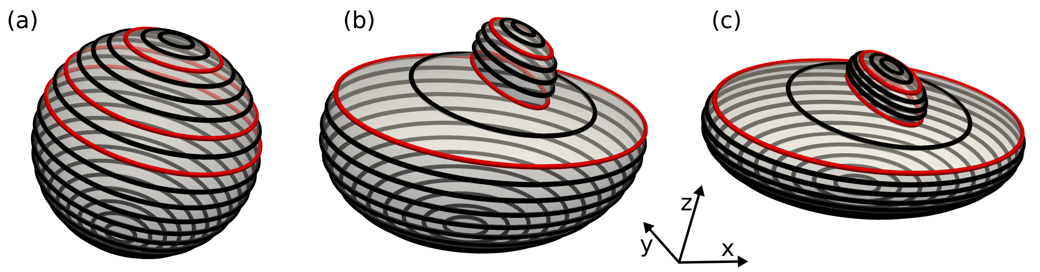


**Figure 1.** Illustration of 3D bodies as a set of 2D polygons. The three red slices are the control polygons which are used to transform the body. (a) Reference model sphere represented as horizontal polygons. (b) Sphere from 1a after transformation with the scaling parameters of table 1. (c) Sphere from 1a after transformation with $Sz = 0.6$ and the scaling parameters of table 1. Inset shows the orientation of the coordinate system.

### 2.3 Subduction Zones

Subduction zones are frequently investigated in geodynamic modeling studies. A central element is the orientation and location of the subducting slab. In this case, it is more convenient to represent the subducting plate as a collection of vertical polygons (Figure 2). We automatically detect the polygon nodes that make up the slab part (red in Figure 2b) and rotate them by angle $\theta$ to change the subduction angle (blue in Figure 2b). For 3D slabs that dip obliquely to the orientation of the coordinate system (Fig-

**Table 1.** Scaling parameters used to transform the sphere in Figure 1a into the shapes in Figures 1b,c. Note that the polygon numbering goes from the bottom to the top. Only the red numbers are free parameters that need to be chosen. The black numbers are generated automatically, depending on the red ones.

| Polygon | $Sx$ | $Sy$ |
|---|---|---|
| 21 | 0.50 | 0.90 |
| ... | 0.50 | 0.90 |
| 19 | 0.50 | 0.90 |
| 18 | 0.45 | 0.83 |
| 17 | 0.40 | 0.75 |
| 16 | 0.35 | 0.68 |
| 15 | 0.30 | 0.60 |
| 14 | 0.90 | 0.80 |
| 13 | 1.50 | 1.00 |
| ... | 1.50 | 1.00 |
| 1 | 1.50 | 1.00 |

ure 2a), we first detect the direction of dip and recalculate $\theta'$ in the plane of the polygons so that the entire slab is rotated correctly. Additional rotation centers can also be placed anywhere along the slab to bend the deeper parts (Figure S5). This can be useful when the dip of the slab is well constrained close to the surface but changes at depth like along the west coast of South America.

Subduction setups often require a weak zone of elevated temperature, lowered viscosity or lowered yield strength to facilitate slip of the slab along the overriding plate. We automatically generate a weak zone of desired thickness following the curvature of the slab from the surface to a desired depth (green in Figure 2). Likewise, we can automatically add oceanic crust of desired thickness to the top of the slab (light blue in Figure 2).

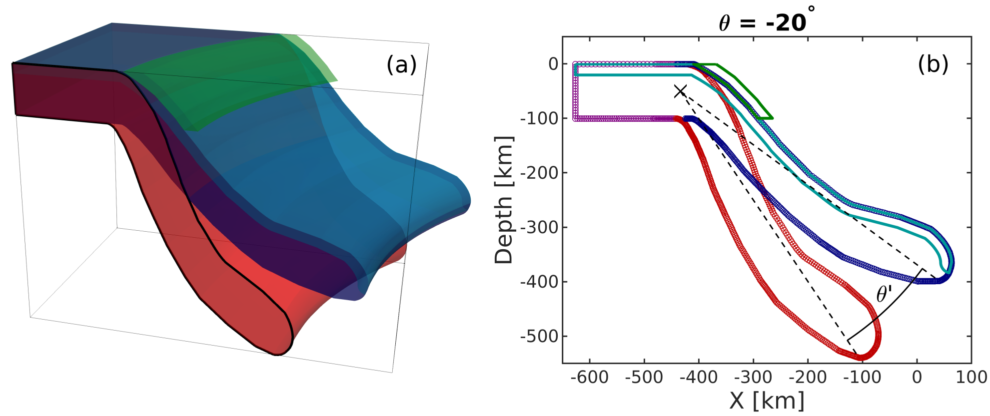


**Figure 2.** (a) 3D Example of a plate, subducting along a curved trench, drawn in geomIO (red) and an automatically generated variation with reduced subduction angle of 20° (blue). Alongside the variation, we can also automatically generate oceanic crust (light blue) and a weak zone (green) between slab and overriding plate. Black line shows one of the vertical polygons that the 3D volume is represented as inside our algorithm and is identical to the red+purple polygon in 2b. (b) Representation of the plates in 2a as a vertical polygons. Original in red, variation in blue, crust in light blue and weak zone in green. Purple nodes belong to both versions. Black cross shows the center of rotation.

## 3 Applications

In this section, we present two examples of applications to geological scenarios. Section 3.1 focuses on fault development associated with a salt diapir in an extending regime, including forward simulations and inversion. In section 3.2, we investigate the dependence of plate velocity on the initial dip angle of a subducting plate and the evolution of the dip angle. Spang et al. (2021) presents a third application in 3D to a magmatic system.

### 3.1 Application I: Salt

Our method is especially useful when constraints from imaging studies are ambiguous like in the case of the Epsilon diapir in Norway (Jackson & Lewis, 2012). After a seismic survey, the stem of the diapir was interpreted to be about 300 m wide (green in Figure 3) but a drilling survey revealed it to be more than 1 km wide instead. Jackson and

Lewis (2012) state that the location of the flanks can move hundreds of meters depending on the interpretation of the survey. The authors present a tear-drop-shaped post-drilling interpretation (dashed purple in Figure 3) of the diapir's extent but acknowledge that most of the margins are still uncertain. Jones and Davison (2014) revisit the data on the Epsilon diapir and present a much straighter interpretation (solid purple in Figure 3).

Here, we use the survey of the Epsilon diapir to show how different initial geometries, within the range of uncertainty of imaging data, can result in vastly different model results. We also demonstrate how geodynamic models with variable initial geometries, supported by other observations, can help reduce ambiguity of imaging studies. Figure 3 shows the reflection profile and various interpretations. Without the information of the drilling survey, the red outline could also be a valid interpretation, so we use it as an initial guess and reference model for our variations. The dashed yellow lines show the location of four control polygons located at the basis, the thinnest (neck) and thickest (head) part of the diapir as well as on the transition from neck to head.

#### *3.1.1 Faulting Patterns in Dependence of Initial Geometry*

Using the red outline in Figure 3 as an initial guess or reference model, we create about 1500 different diapirs. For each variation, we generate a set of scaling parameters ($S_1$ to $S_4$) to be applied at the control polygons as well as one parameter ($Sz$) to vary the height of the diapir. Because it is a 2D example, $S_1$ to $S_4$ are equivalent to $Sx_1$ to $Sx_4$ and there are no $Sy$ parameters. We generate the scaling parameters on a regular grid within the ranges given in table S3 and add random noise to sample the parameter space. The reference depth for scaling in the vertical direction is the base of the diapir.

We then model the evolution of each diapir in an extensional geodynamic setting for 100 kyrs, using the thermomechanical code LaMEM (Kaus et al., 2016). We employ a linear-visco-elasto-plastic rheology and a density contrast of 500 $\mathrm{kg\,m^{-3}}$. A more detailed description of the code and the material parameters can be found in supplementary text S3.

From the model output, we binarize the accumulated plastic strain to automatically identify faults that developed to accommodate the extension. With the help of prin-

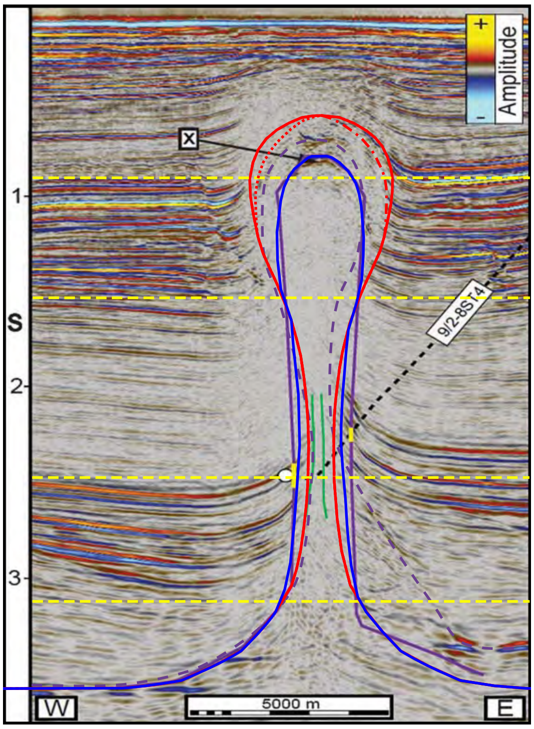


**Figure 3.** Seismic reflection profile of the Epsilon diapir modified from Jones and Davison (2014). Green lines show pre-drilling interpretation, dashed purple, post drilling interpretation of Jackson and Lewis (2012) and solid purple post-drilling interpretation of Jones and Davison (2014). Red line shows our symmetric initial guess and reference model. Dotted and dashed-dotted red lines show mirrored variations of red to test the effect of asymmetry. Solid blue line shows our synthetic 'true' geometry that we try to fit in section section 3.1.2. Dashed yellow lines show location of control polygons.

ciple component analysis, we extract preferred orientation ($\alpha$), length ($l$), aspect ratio ($r$) and the location ($x, z$) of the faults or fault systems. The aspect ratio of faults is computed by taking the ratio between the magnitudes of their two principle components (i.e. Eigenvalues).

#### *3.1.2 Inverting for Geometry*

With a parameterized geometry, it is possible to invert for the unknown structure of the diapir with the help of an observable. Using a scaling parameter set of 1.2, 2.0, 0.8, 0.6 ($\mathrm{S}_1 - \mathrm{S}_4$) and 0.94 (Sz), we produce a synthetic diapir (blue in Figure 3) similar to the interpretation of (Jones & Davison, 2014). We then forward model the evolution of this diapir in an extensional setting for 100 kyrs which results in a single normal fault (Figure 4a). The size, location and orientation of that fault might be visible in a seismic study (Juhlin et al., 2010) and could serve as an observable which we can use to constrain the diapir geometry through inversion.

We compare the faults developed by the 1500 variations to our synthetic observation (fault in Figure 4a, developed by the blue diapir in Figure 3). After identifying the 50 best fitting models, we create 8 new variations with similar parameters for each one to improve our coverage in the area of low misfit (Sambridge, 1999, Neighborhood algorithm). This procedure is commonly used to deal with non-linear and -unique inverse problems (e.g. Baumann & Kaus, 2015) and is repeated four times here, yielding a final ensemble of about 3100 variations. After 2 iterations, it was clear that the minimum for $Sx_4$ was close to our initial lower bound of 0.5 (table S3) and we relaxed the bound to 0.25 for the 3rd and 4th iteration of the neighborhood algorithm.

We also perform a second inversion, using only 2 control polygons (locations are shown in Figure 6) alongside vertical scaling to investigate how robust the approach is. Because of the smaller parameter space, we test an initial set of about 500 variations and then add $4 \times 400$ variations with the neighborhood algorithm for the 2 control polygon case.

Computing a misfit between two geometric observations is not as straight forward as comparing numeric outputs and observations. To address this issue, Wijns et al. (2003) used human appraisal to rank modeled faulting patterns, while Boschetti et al. (2003) utilized self organizing maps to do the same. We compute the misfit of an individual fault pattern, by combining some of the geometric properties of the modeled fault and comparing them to our synthetic observation:

$$\Phi_i = \left( \frac{\sqrt{(|x_i| - |x_o|)^2 + (z_i - z_o)^2}}{l_n} + \frac{||\alpha_i| - |\alpha_o||}{\alpha_n} + \frac{|r_i - r_o|}{r_n} \right) \times N \tag{4}$$

$\Phi_i$ is the misfit of a fault to our synthetic observation. Subscript $i$ corresponds to the geometry variation, subscript $o$ to the synthetic observation and subscript $n$ to a normalization constant for each property. The first term of the right hand side compares the location of the fault centers with $x$ corresponding to the lateral and $z$ to the vertical coordinate. $\alpha$ is the angle between the fault and the horizontal direction and $r$ the aspect ratio of the fault. $N$ is the number of faults that develop. $l_n$ is 2 km, a tenth of the model width, $\alpha_n$ is 5° and $r_n = r_o$. These parameters were chosen to make sure that all three right hand side terms are in the range of 0 to 1 for the majority of models. Figure 4 shows how large each of the three terms of equation 4 are for 8 selected fault systems.

We decided to use the absolute values of $x$ and $\alpha$ as section 4.1.1 suggests that the side, to which the faults develop, is not coupled to the geometry but is related to how the curved diapir boundaries intersect with the rectangular grid. This is supported by the fact that the issue persists at higher resolution models and disappears for the asymmetric cases (supplementary text S4 and Figure S8).

### 3.2 Application II: Subduction

We use the method introduced in section 2.3 to test the dependence of plate velocity on the initial dip angle ($\beta_0$) of the subducting slab. Using a reference model, dipping with 60°, we test 16 variations in the range of 30° to 90°. We use a simple 2D model with an oceanic plate of 70 km thickness (corresponding to a thermal age of 30 Myr) subducting underneath a continent of 100 km thickness. Both plates are free (i.e. not fixed to the edges of the model) and as we do not prescribe any boundary velocities, the movement of the plates in entirely driven by the negative buoyancy of the cold slab. We test models with a 20 km (4 cells) and 30 km (6 cells) wide weak zone. Supplementary text S3 provides more details on the setup and the thermomechanical code we use.

## 4 Results

### 4.1 Application I: Salt

#### *4.1.1 Faulting patterns in Dependence of Initial Geometry*

To accommodate the extension, the models start developing faults at the tip of the diapir as well as the surface. The faults then grow from the surface downwards or from the dipir upwards and eventually connect both (supplementary Figure S6). In the majority of cases, the strain then focuses on one of the two directions and a single fault forms, taking up most of the deformation. Both sides were preferred in a large number of models for all heights of diapirs (Figure 4b,c). In about 25% of the cases, the fault did not connect to the center of the diapir, but instead it formed at the edges of the diapir top

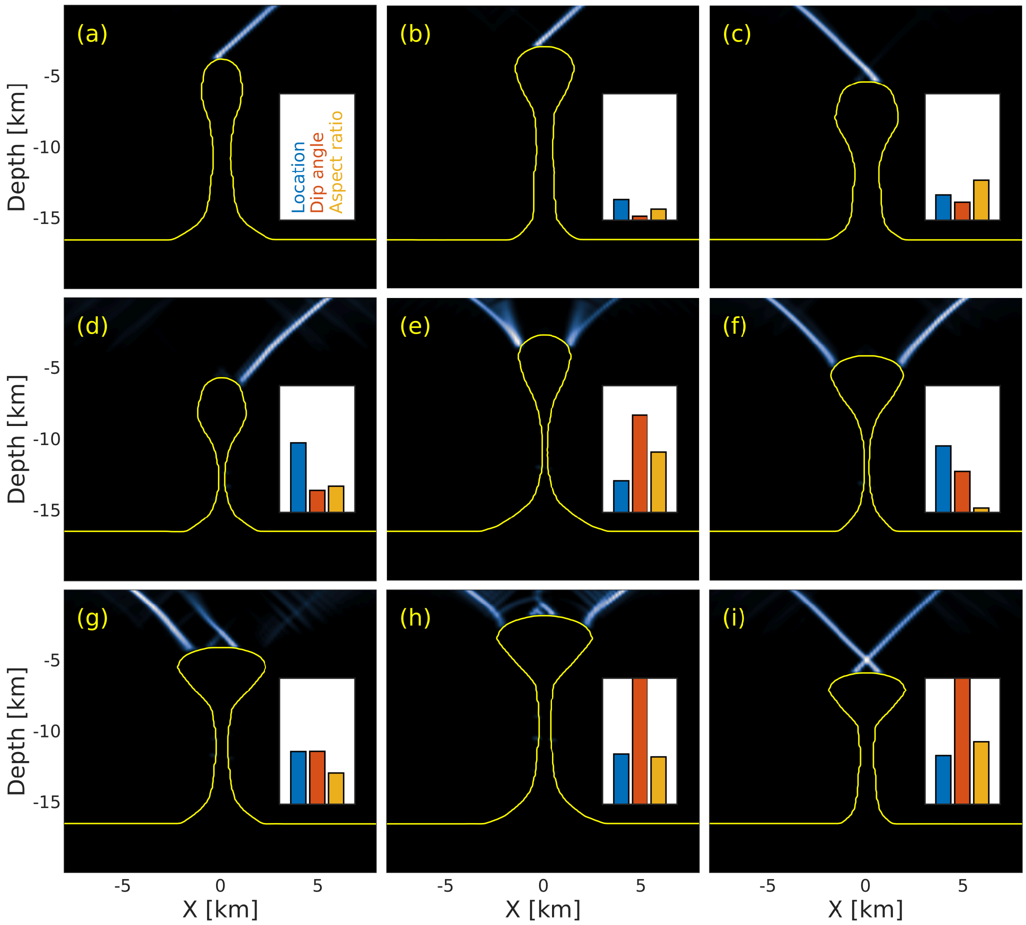


**Figure 4.** Accumulated plastic strain after 100 kyrs corresponding to normal faults that formed to accommodate the extension of the model. (a) Synthetic 'true' diapir (blue in Figure 3) and corresponding fault which serves as our synthetic observation, other faults are compared to (eq. 4). (b and c) 'Regular case': Deformation focuses on a single fault for different diapir heights. This happens for the majority of cases. (d) Deformation focuses on a single fault but the fault does not start at the center of the diapir top. (e) Deformation is not taken up by a single fault but two areas with a lot of small faults. (f) Faults form on both sides of the diapir. (g) Two parallel faults form with some minor opposite ones. (h) A large number of smaller faults develop. (i) Model develops two crossing faults. Insets show misfit of the observed fault/fault system to the synthetic observation in 4a. Blue bar corresponds to the location term, orange to the orientation term and yellow to the aspect ratio term of equation 4.

(Figure 4d–h). For some tall diapirs, the deformation did not focus on a single fault but was distributed over an area close to the surface (Figure 4e). In some cases, one dominant fault formed, but a part of the deformation was also accommodated by other parallel and opposite faults (Figure 4g,h). In few cases, two faults formed that shared the strain between them (Figure 4f,i).

Figure 5 shows a selection of geometric fault properties in dependence of the scaling parameters applied to the diapir. Supplementary Figure S7 shows all relations between scaling parameters and fault properties. Intuitively, there is a good correlation between the height of diapir ($Sz$) and the depth of the lower end of the fault as the fault connects the top of the diapir to the surface (Figure 5a). It is, however, evident that there is some spread towards deeper fault tips as well. This deviation represents cases where the fault does not start at the tip or center of the diapir, but instead to one of the sides (Figure 4d–h). We use the relation between $Sz$ and the depth of the fault tip to discriminate between faults that connect to the center of the diapir (blue in Figure 5) and faults that connect to the sides (orange).

The aspect ratio scales similarly with $Sz$ as the depth of the fault tip because long faults are not wider than short faults (Figure 5b). The spread is a bit bigger and there are more anomalous cases. Where $Sz$ and $r$ are small, two crossing faults developed (Figure 4i) and the image processing was not able to properly split them, returning flawed values for the width. Cases of low $r$ and large $Sz$ relate to those shown in Figure 4e,h and predominantly happen when the faults do not form in the center of the diapir (orange in Figure 5b).

Figure 5c shows that most faults have an angle of roughly 50 degrees. It also shows a striking dependence of the fault location on $S_2$ (the neck of the diapir). For small $S_2$, the faults form almost exclusively to the sides of the diapir (orange) while they occur predominantly in the center (blue) for high $S_2$. Overall, more faults extend to the right. Given that the diapirs are symmetric, this may be due to small asymmetries that arise from gridding.

Figure 5d relates the width of the diapir head ($S_4$) and the lateral coordinate of the fault center. It shows that the faults form further from the center of the domain, the wider the diapir is. This is the only correlation for $S_4$ (Figure S7). The figure also clearly shows the two different trends of faults forming in the center or at the sides of the di-

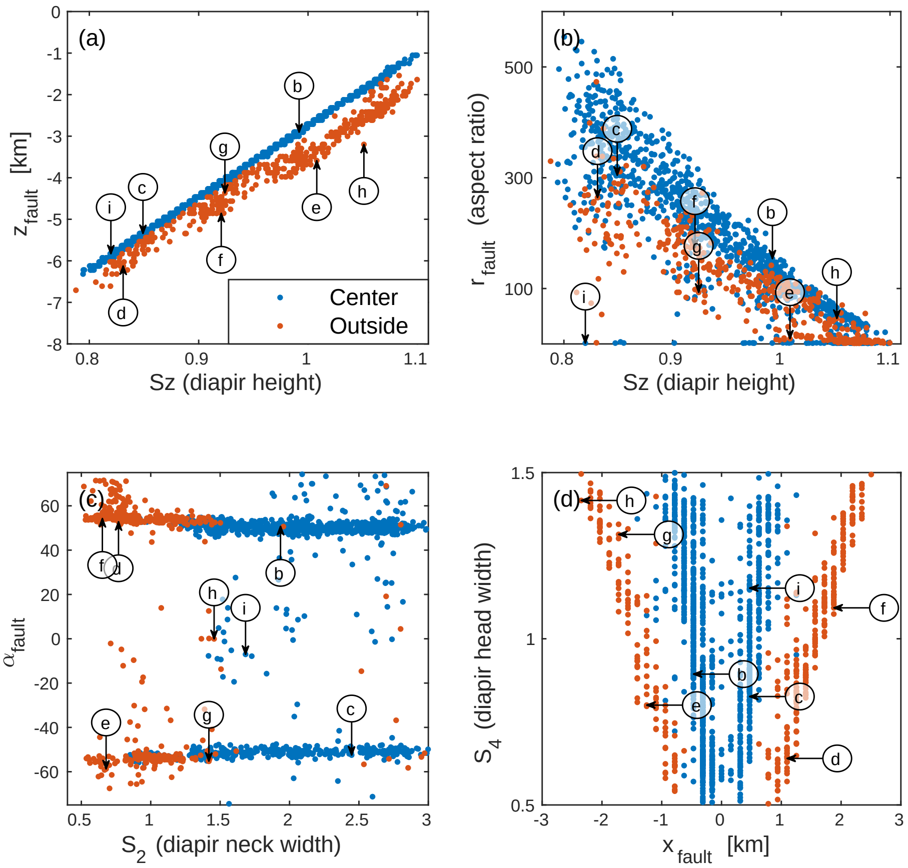


**Figure 5.** Different fault properties ($\alpha$, r, x, z) in relation to scaling parameters. Arrows show where the examples in Figure 4b–i plot to relate fault types with the parameters. (a) Depth of the lower end of the fault in dependence of $Sz$. This allows for the distinction between faults that start from the center (blue) and faults that start from at the side (orange) of the diapir. Same color code in b–d. (b) Fault aspect ratio in dependence of $Sz$. (c) Fault orientation in dependence of $S_2$. $\alpha < 0$: fault goes to the left. (d) Lateral position of the fault center in dependence of $S_4$.

apir head with few exceptions. $S_1$ (width of the diapir base) and $S_3$ (width at transition zone from neck to head of the diapir) do not show any correlation with any of the faults' geometric properties (Figure S7).

We also tested two sets of models with the same scaling parameters but a slightly asymmetric reference model (red dotted and red dashed-dotted in Figure 3). The results are presented in supplementary text S4 and Figure S8.

#### *4.1.2 Inverting for Geometry*

After four iterations of the neighborhood algorithm, we have a total of 3100 models. Figure 6a shows the 200 diapirs that develop faults with the lowest misfit in comparison with the synthetic observation (fault in Figure 4a). All 200 are almost a perfect match for the head of the diapir in terms of height and shape. The transition between head and neck of the diapir shows very large spread over almost the entire range of possible extents. The neck and base of diapir show less spread but are not as well constrained compared as the top of the diapir.

Figure 6b shows the misfit of each model in dependence of the two most important parameters, the width of the diapir head ($S_4$) and the height of the diapir ($Sz$). $Sz$ is the most well defined parameter with models outside the range of 0.9 to 1.0 showing large misfit. But inside that range, there is also a correlation between misfit and $S_4$ with the minimum in the area of 0.6. As the location of this minimum is very close to our lower bound for $Sx_4$, we extended it from 0.5 to 0.25 for the last 2 iterations of the neighborhood algorithm.

Figures 6c and 6d show the results of attempting the same inversion by only using 2 control polygons instead of 4 alongside vertical scaling to fit the synthetic observation. Again, the height and upper part of the head as well as the thickness of the diapir neck are well constrained. Most low-misfit geometries have a kink at 7 km depth which is the result of fitting both the shape of the head and width of the neck with only 2 control polygons. Furthermore, none of the low-misfit models have the correct width of the diapir base.

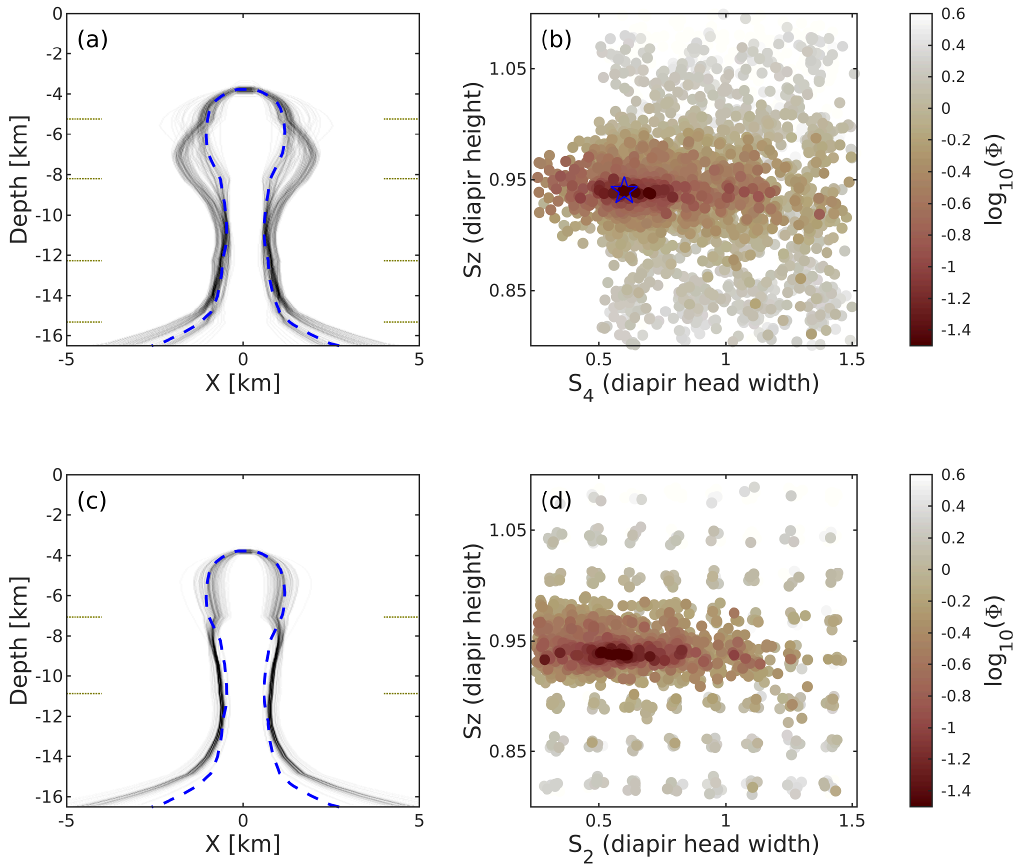


**Figure 6.** (a) Synthetic diapir in dashed blue (solid blue in Figure 3) and the 200 variations out of 3100 with the smallest misfit in gray. Dots on the sides indicate locations of the 4 control polygons. (b) Misfit ($\log_{10}(\Phi)$) as a function of width of the diapir head ($S_4$) and height of the diapir ($Sz$). Note the denser distribution of samples around the minimum courtesy of the neighborhood algorithm. Blue star indicates the location of the synthetic 'true' geometry (dashed blue in 6a). Figure S9 shows misfit as a function of all parameter combinations. (c) Similarly to 6a, Top 200 out of 2100 variations, using 2 control polygons. (d) Misfit as function of diapir height and head width for the 2 control polygon example.

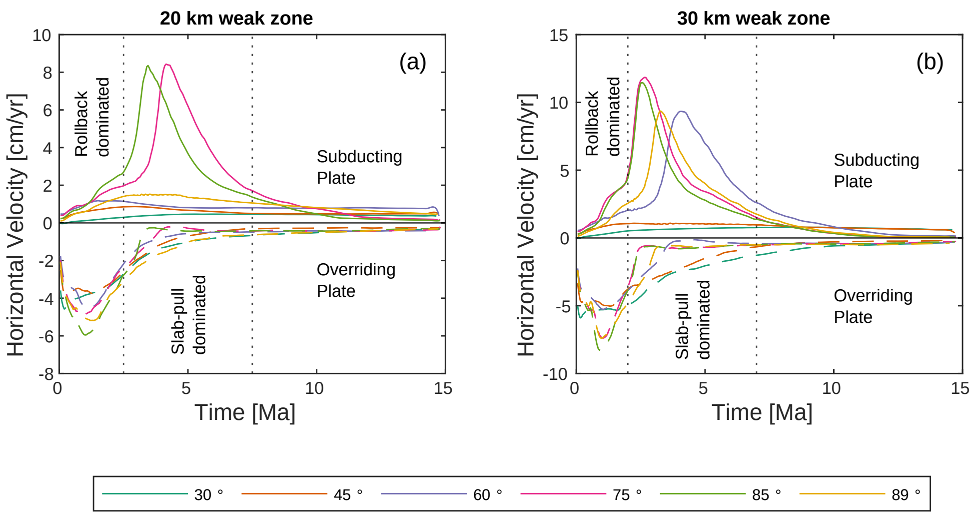


**Figure 7.** Average velocity of subducting (solid lines in upper panel) and overriding plate (dashed lines in lower panel) in dependence of time for a selection of different initial slab angles ($\beta_0$). Dotted vertical lines indicate periods dominated by different mechanisms. Within the first 2.5 Myr, the convergence is mostly accommodated by slab rollback and trench retreat. In the following 5 Myr, it is dominated by the trenchward motion of the subducting plate. (a) Models have a weak zone that is 20 km wide (about 4 grid cells). (b) Models have a weak zone 30 km wide (about 6 grid cells).

## 4.2 Application II: Subduction

All subduction models start out with an initial stage of slab rollback, trench retreat and continent extension while the slab starts sinking. Over time, the horizontal velocity of the suducting plate increases depending on the angle of the slab (Figure 7). Models that start with a steep subduction angle ($\beta_0 > 65°$) eventually reach a stage where velocities increase strongly and the trench reverses direction and starts to advance towards the continent, leading to shortening of the fore-arc. Once the slab approaches the bottom of the model, velocities decrease again. This also stops the advance of the trench, leading to another rollback period.

### *4.2.1 Convergence Velocity*

In Figure 8a, we show the difference between the average horizontal velocities of subducting and overriding plate (i.e. the convergence velocity) as a function of time and

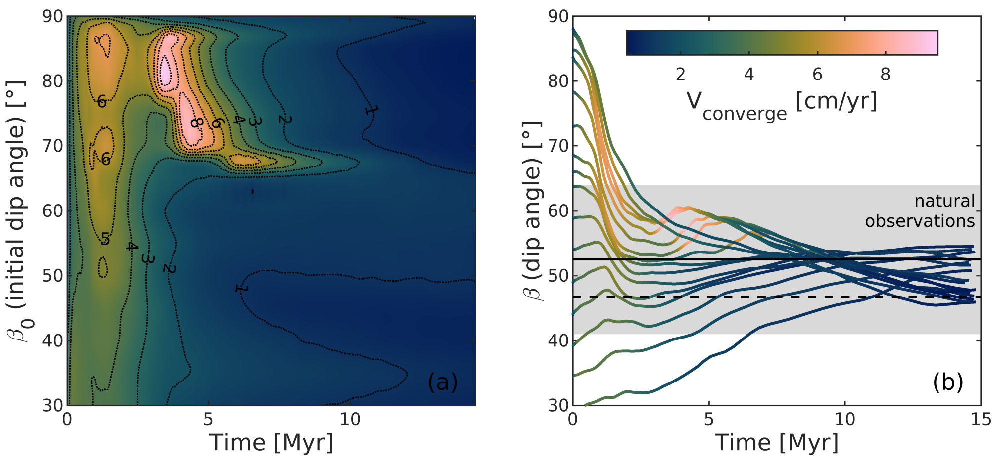


**Figure 8.** (a) Convergence rate between oceanic and continental plate in dependence of initial subduction angle ($\beta_0$) through time. (b) Dip angle of the subducting slab ($\beta$) as a function of time for all models. Color gradient along the curves shows convergence velocity. Solid black line shows global average of dip angles from Lallemand et al. (2005) and shaded gray area indicates one standard deviation. Dashed black line shows global average of dip angles from Syracuse and Abers (2006).

initial subduction angle $\beta_0$. Within the first 2 Myr, all models undergo a period of convergence with maximum velocities of 4 cm yr$^{-1}$ for low $\beta_0$ and 7 cm yr$^{-1}$ for high $\beta_0$. In this period, the convergence velocity is mainly caused by the retreat of the trench (see also Figure 7). For $\beta_0 <= 65°$, the convergence rate then slowly declines over time. However, models that start with a steeper slab go through a second period of rapid acceleration after about 4 Myr, reaching up to 9 cm yr$^{-1}$ at $\beta_0 = 80°$ before declining as well. In this period, the velocity of the subducting plate is the main contributor to the convergence velocity (Figure 7). While velocities generally increase with $\beta_0$, they drastically decrease again at $\beta_0 > 85°$ as we approach a vertical initial slab. Supplementary text S5 presents an example of how a velocity profile (e.g., Sdrolias & Müller, 2006) can be used to invert for the initial subduction angle $\beta_0$ similar to section 4.1.2.

Models with a wider weak zone (30 km instead of 20 km) show the same general behavior, but the velocity of both plates is higher. There are also more models that enter the second phase of acceleration (Figure 7).

#### *4.2.2 Subduction Angle*

Figure 8b shows the evolution of the dip angle for all models. While slabs that start out with a shallow dip angle gradually steepen over time, slabs that start steep quickly undergo flattening until leveling out at about 60°. Models that undergo a second phase of acceleration (see Figure 8a) slightly steepen from 55° to 65° during that period again. Once the slabs start approaching the bottom of the model (660 km depth), they flatten towards 45°. All models converge to a dip angle between 45° and 55° which is agreement with global averages as reported by Lallemand et al. (2005) and Syracuse and Abers (2006).

## 5 Discussion

### 5.1 Parameterization and Transformation

The method we present in this study is based on two main concepts. The use of a reference geometry (sphere in section 2.2 and Figure 1, red plate in section 2.3 and Figure 2, red outline in section 3.1 and Figure 3, $\beta_0 = 60°$ model in section 3.2) and control polygons/rotation centers that act as anchors for the transformation.

#### *5.1.1 Strengths and Weaknesses*

Using a reference geometry removes the necessity to define a large number of coordinates for every new variation. Instead, each complex shape is represented by a small number of values that describe how it is different to the reference geometry. This comes at the price of limiting the shape of possible variations. It would for instance not be possible to make the diapir in Figure 3 lean towards one side, introduce any asymmetry (in the x-y-plane) that was not present before or split the head in two without creating a new reference model with those features. But since the initial geometry of geodynamic models is commonly constrained by imaging surveys, there usually is enough information to create an appropriate reference model of the geological unit (Figure 3).

The use of control polygons and interpolation between them allows us to greatly reduce the number of necessary parameters compared to providing scaling parameters for each polygon or changing individual coordinates/vertices. Homogeneous three-dimensional scaling of the body is possible with a single control polygon and parameter ($Sx = Sy = Sz$). At the same time, complex changes as shown in Figure 1 can be achieved with only 6 or 7 parameters. Free choice of the position of the control polygons allows for great flexibility. The closer control polygons are to another, the shorter the wavelength of variation. If a part of the geological unit is well constrained, this part can be kept locked by bounding it with two control polygons with constant scaling parameters of 1, while the other parts can stay variable. As mentioned before, our transformations cannot introduce additional complexity into the individual polygons.

Figure 6c illustrates that using a smaller number of control polygons (2 instead of 4) can be sufficient to fit the most influential features of the diapir. But it also demonstrates a potential pitfall of using few control polygons. Because the observation (fault system) is sensitive to the neck width but not the base width (Figures 6a and S7) but both features are governed by the same control polygon, the base of the diapir appears to be well constrained but is actually wrong (Figure 6c). It is important to keep in mind that each control polygon should only govern one feature of a body.

#### *5.1.2 Relation to other Approaches*

Our approach shares similarities with that of (Sevilla et al., 2020) which also applies 2D transformations at different levels of the third dimension that control how the entire 3D shape is transformed. Both methods seem capable of producing similar transformations with the same number of parameters but we consider the scaling parameters to be more intuitive than the control points of NURBS surfaces.

There is also similarity to the work of (Galley et al., 2020) as groups of surface nodes are moved together to preserve smooth surfaces while other groups of nodes remain stationary. In the case of the diapir (Figure 3) we can change height and width at 4 levels with only 5 parameters whereas moving a single surface vertex in 2D already requires 2 parameters. The approach of (Galley et al., 2020) does in turn provide more flexibility to introduce asymmetric features.

Our adaptation for subduction zones shares the philosophy of using a combination of arbitrary coordinates (provided by the Inkscape drawing) and features that are specific to subduction zones like dip angle and plate thickness with the GWB (Fraters et al., 2019). The main difference is the use of a reference geometry which means that weak zone, crust and flattening/steepening segments can be added with one or two parameters each instead of building the plate out of individual segments each requiring 3 or more parameters. By not relying on a reference geometry, the GWB has advantages in quickly introducing big geometry changes.

### 5.2 Importance of Initial Geometry

Both applications (more details in the following sections) demonstrate that different initial geometries within the range of uncertainty of geophysical imaging can lead to drastically different modeling results. Therefore, it is crucial to test different setups and develop an understanding of the influence that the geometry of the geological structures can have. While this finding is not necessarily new as previous studies have highlighted the dependence of results on initial geometry (e.g. Le Pourhiet et al., 2003; Duretz et al., 2020), the issue often remains unaddressed in many state-of-the-art geodynamic studies (see section 1) that use a single geometry or a handful of end-member cases without parameterization (e.g. Liao et al., 2017; Tetreault & Buiter, 2012).

Our approach enables the user to quickly, on the order of a second per version, and automatically create any number of variations of a complex 3D body in their model. This not only allows for the incorporation of uncertain constraints but can also reveal unexpected dependencies of the model results on the initial geometry of the model. The scaling parameters even facilitate a quantitative description of such dependencies.

### 5.3 Application to Salt

Figure 4 shows how different initial salt geometries result in distinctly different faults. We observe some intuitive relationships like the link between height of the diapir and position or aspect ratio of the fault (Figure 5a,b). But, we also find unexpected correlations like a thin diapir neck facilitating faults at the sides of the diapir (Figure 5c). We also learn that the base of the diapir ($S_1$) and the transition from head to neck ($S_3$) have little to no impact on the developing faults and could therefore be kept constant in further investigations of the system.

It is apparent that faults can develop to both sides of the diapir independently of the geometry for the symmetric case. For the asymmetric case, faults that develop at the side of the diapir head exclusively appear on the side that has a stronger curvature (Figure S8c,f). We tested the asymmetry on both sides to exclude the possibility that this effect is caused by our grid discretization.

Finally, we can see that, given the observation of a fault and a good understanding of the material parameters, geodynamic modeling could help improve imaging results and reduce ambiguity regarding the extent of a diapir. Figure 6 shows that it is in principle possible to constrain the height and head width of the diapir with the help of an observed fault while deeper structures that have no influence of the faulting pattern remain blurred. Applying this to a natural example would involve more unknowns like the material parameters of salt and crust, additional crustal layers, heterogeneities in the salt and topography, resulting in a larger parameter space to consider. However, geometry, parameterized by scaling parameters, can be included in such a study (Spang et al., 2021).

### 5.4 Application to Subduction

Figures 7 and 8a show how strongly the velocity of plates and the entire dynamics of the model depend on the initial angle of the subducting slab. While models with an initial angle $\beta_0 <= 65°$ move at relatively even velocities throughout 15 Myr, models with steeper slabs run through a period of strongly increasing velocities that are high enough to stop or even reverse the retreat of the trench. The timing and maximum velocity of this phase of acceleration also depend on the initial geometry of the model.

Another geometrical parameter that strongly influences the velocities of the plates is the thickness of the weak zone between subducting and overriding plate (Figure 7). With a thicker weak zone, there is less friction between the plates and they reach higher velocities. So, both parameters (initial dip angle of the slab and thickness of the weak zone) can exert a first order control on the model dynamics and could overprint a lot of other effects. With our method, it is easy to change either parameter and investigate their influence on the model results without investing a lot of time into creating different initial geometries.

Figure 8b shows that independently from the initial subduction angle ($\beta_0$), all models converge to a similar angle of about 50° after a few Myr. This range is in agreement with global averages of subucting slabs (Lallemand et al., 2005; Syracuse & Abers, 2006) which suggests that 50° is the preferred angle for long-term slab-pull-dominated subduction.

## 6 Conclusion

In this study, we present a simple and intuitive method to describe and manipulate 3D bodies in a heterogeneous manner with a limited set of parameters. This not only allows us to include uncertainties about initial geometry in the modeling process, but also enables us to quantify the relationship between initial geometry of a model and the computed output. As shown by our study and Spang et al. (2021), this allows us to even improve constraints on geometry by integrating different observations and invert for geometric properties.

We present two application examples. (i) A salt diapir with an ambiguous geometry in seismic imaging. We show that slight geometric variations that would all satisfy the imaging data, can result in the development of vastly different faulting patterns in an extending regime. It is also evident that small asymmetries in the diapir lead to distinctive differences in the developing faults around the diapir. Furthermore, we show that, with our parameterization, initial geometry can be treated like any material parameter and included in sensitivity studies or inversion frameworks. (ii) A subduction zone where we vary the initial dip angle of the subducting slab as well as the thickness of the weak zone between subducting and overriding plate. Both parameters influence the velocity evolution of the plates by an order of magnitude. We show that, independently of the initial dip angle, all slabs approach a subduction angle of about 50°.

Our study presents an intuitive method to parameterize and manipulate the initial geometry of geodynamic models and highlights the importance of considering different geometries instead of using just one. We implemented the method as a tool in the open-source software package geomIO which is fully compatible with the open-source, thermomechanical stokes code LaMEM. Areas of application include salt tectonics, subduction settings, volcanic systems with varying sizes/shapes of magma bodies and models of orogenesis with uncertain extents of critical units. As geomIO can forward model Bouguer anomalies, constraints from gravity surveys can directly be considered in the creation of the initial geometry of geodynamic models.

**Acknowledgments**

The authors thank John Naliboff, Florian Wellmann and one anonymous reviewer for their help in improving the quality of the manuscript. This study was funded by the European Research Council through the MAGMA project, ERC Consolidator Grant # 771143. We used perceptually uniform colormaps to prevent optical data distortion (Crameri, 2018). Parts of this research were conducted using the supercomputer Mogon II and/or advisory services offered by Johannes Gutenberg University Mainz (hpc.uni-mainz.de), which is a member of the AHRP (Alliance for High Performance Computing in Rhineland Palatinate, www.ahrp.info) and the Gauss Alliance e.V..

## Open Research Section

Software used for this research is available on zenodo at: https://doi.org/10.5281/zenodo.6472320 (Kaus et al., 2016; Bauville & Baumann, 2019)

## References

Alisic, L., Gurnis, M., Stadler, G., Burstedde, C., Wilcox, L. C., & Ghattas, O. (2010). Slab stress and strain rate as constraints on global mantle flow. *Geophysical Research Letters*, *37*(22).

Baumann, T. S., & Kaus, B. J. P. (2015). Geodynamic inversion to constrain the non-linear rheology of the lithosphere. *Geophysical Journal International*, *202*(2), 1289–1316.

Baumann, T. S., Kaus, B. J. P., & Popov, A. A. (2014). Constraining effective rheology through parallel joint geodynamic inversion. *Tectonophysics*, *631*, 197–211. doi: https://doi.org/10.1016/j.tecto.2014.04.037

Bauville, A., & Baumann, T. S. (2019). geomIO: an open-source MATLAB toolbox to create the initial configuration of 2-D/3-D thermo-mechanical simulations from 2-D vector drawings. *Geochemistry, Geophysics, Geosystems*, *20*(3), 1665–1675. doi: https://doi.org/10.1029/2018GC008057

Beucher, R., Moresi, L., Giordani, J., Mansour, J., Sandiford, D., Farrington, R., ... others (2019). UWGeodynamics: A teaching and research tool for numerical geodynamic modelling. *Journal of Open Source Software*, *4*(36), 1136.

Bosch, M., Mukerji, T., & Gonzalez, E. F. (2010). Seismic inversion for reservoir properties combining statistical rock physics and geostatistics: A review. *Geophysics*, *75*(5), 75A165–75A176.

Boschetti, F., Wijns, C., & Moresi, L. (2003). Effective exploration and visualization of geological parameter space. *Geochemistry, Geophysics, Geosystems*, *4*(10).

Caumon, G., Collon-Drouaillet, P., Le Carlier de Veslud, C., Viseur, S., & Sausse, J. (2009). Surface-based 3D modeling of geological structures. *Mathematical Geosciences*, *41*(8), 927–945.

Čížková, H., & Bina, C. R. (2015). Geodynamics of trench advance: Insights from a Philippine-Sea-style geometry. *Earth and Planetary Science Letters*, *430*, 408–415.

Crameri, F. (2018). Scientific colour-maps. *Zenodo*, *10*. doi: 10.5281/zenodo.1243862

Duretz, T., Asti, R., Lagabrielle, Y., Brun, J.-P., Jourdon, A., Clerc, C., & Corre, B. (2020). Numerical modelling of Cretaceous Pyrenean Rifting: The interaction between mantle exhumation and syn-rift salt tectonics. *Basin Research*, *32*(4), 652–667.

Frank, T., Tertois, A.-L., & Mallet, J.-L. (2007). 3D-reconstruction of complex geological interfaces from irregularly distributed and noisy point data. *Computers & Geosciences*, *33*(7), 932–943.

Fraters, M., Thieulot, C., Van Den Berg, A., & Spakman, W. (2019). The Geodynamic World Builder: a solution for complex initial conditions in numerical modeling. *Solid Earth*, *10*(5), 1785–1807.

Fullagar, P. K., Hughes, N. A., & Paine, J. (2000). Drilling-constrained 3D gravity interpretation. *Exploration Geophysics*, *31*(2), 17–23.

Galley, C. G., Lelièvre, P. G., & Farquharson, C. G. (2020). Geophysical inversion for 3d contact surface geometry. *Geophysics*, *85*(6), K27–K45.

Guillen, A., Courrioux, G., Calcagno, P., Lane, R., Lees, T., & McInerney, P. (2004). Constrained gravity 3D litho-inversion applied to Broken Hill. *ASEG Extended Abstracts*, *2004*(1), 1–6.

Jackson, C. A.-L., & Lewis, M. M. (2012). Origin of an anhydrite sheath encircling a salt diapir and implications for the seismic imaging of steep-sided salt structures, Egersund Basin, Northern North Sea. *Journal of the Geological Society*, *169*(5), 593–599. doi: 10.1144/0016-76492011-126

Jadamec, M. A., Billen, M. I., & Roeske, S. M. (2013). Three-dimensional numerical models of flat slab subduction and the Denali fault driving deformation in south-central Alaska. *Earth and Planetary Science Letters*, *376*, 29–42.

Jessell, M. (2001). Three-dimensional geological modelling of potential-field data.

*Computers & Geosciences*, *27*(4), 455–465.

Jones, I. F., & Davison, I. (2014). Seismic imaging in and around salt bodies. *Interpretation*, *2*(4), SL1–SL20. doi: 10.1190/INT-2014-0033.1

Juhlin, C., Dehghannejad, M., Lund, B., Malehmir, A., & Pratt, G. (2010). Reflection seismic imaging of the end-glacial Pärvie Fault system, northern Sweden. *Journal of Applied Geophysics*, *70*(4), 307–316.

Kaus, B. J. P., Popov, A. A., Baumann, T., Pusok, A., Bauville, A., Fernandez, N., & Collignon, M. (2016). Forward and inverse modelling of lithospheric deformation on geological timescales. In *Proceedings of NIC Symposium.*

Lallemand, S., Heuret, A., & Boutelier, D. (2005). On the relationships between slab dip, back-arc stress, upper plate absolute motion, and crustal nature in subduction zones. *Geochemistry, Geophysics, Geosystems*, *6*(9).

Le Pourhiet, L., Burov, E., & Moretti, I. (2003). Initial crustal thickness geometry controls on the extension in a back arc domain: Case of the Gulf of Corinth. *Tectonics*, *22*(4).

Liao, J., Gerya, T., Thielmann, M., Webb, A. A. G., Kufner, S.-K., & Yin, A. (2017). 3D geodynamic models for the development of opposing continental subduction zones: The Hindu Kush–Pamir example. *Earth and Planetary Science Letters*, *480*, 133–146.

Moresi, L., Dufour, F., & Mühlhaus, H.-B. (2002). Mantle convection modeling with viscoelastic/brittle lithosphere: Numerical methodology and plate tectonic modeling. *Pure and applied Geophysics*, *159*(10), 2335–2356.

Oldenburg, D., & Pratt, D. (2007). Geophysical inversion for mineral exploration: A decade of progress in theory and practice. In *Proceedings of exploration* (Vol. 7, pp. 61–95).

Pearse, J., & Fialko, Y. (2010). Mechanics of active magmatic intraplating in the rio grande rift near socorro, new mexico. *Journal of Geophysical Research: Solid Earth*, *115*(B7).

Pereyra, V. (1996). Modeling, ray tracing, and block nonlinear travel-time inversion in 3D. *Pure and Applied Geophysics*, *148*(3), 345–386.

Ratnaswamy, V., Stadler, G., & Gurnis, M. (2015). Adjoint-based estimation of plate coupling in a non-linear mantle flow model: theory and examples. *Geophysical Journal International*, *202*(2), 768–786.

Reuber, G. S., Kaus, B. J. P., Popov, A. A., & Baumann, T. S. (2018). Unraveling the physics of the Yellowstone magmatic system using geodynamic simulations. *Frontiers in Earth Science*, *6*, 117. doi: 10.3389/feart.2018.00117

Sambridge, M. (1999). Geophysical inversion with a neighbourhood algorithm-I. Searching a parameter space. *Geophysical Journal International*, *138*(2), 479-494. doi: 10.1046/j.1365-246X.1999.00876.x

Schaaf, A., de la Varga, M., Wellmann, F., & Bond, C. E. (2021). Constraining stochastic 3-D structural geological models with topology information using approximate Bayesian computation in GemPy 2.1. *Geoscientific Model Development*, *14*(6), 3899–3913.

Sdrolias, M., & Müller, R. D. (2006). Controls on back-arc basin formation. *Geochemistry, Geophysics, Geosystems*, *7*(4).

Sevilla, R., Zlotnik, S., & Huerta, A. (2020). Solution of geometrically parametrised problems within a cad environment via model order reduction. *Computer methods in applied mechanics and engineering*, *358*, 112631.

Spang, A., Baumann, T., & Kaus, B. (2021). A Multiphysics approach to constrain the dynamics of the Altiplano-Puna magmatic system. *Journal of Geophysical Research: Solid Earth*, *126*(7), e2021JB021725.

Syracuse, E. M., & Abers, G. A. (2006). Global compilation of variations in slab depth beneath arc volcanoes and implications. *Geochemistry, Geophysics, Geosystems*, *7*(5).

Tetreault, J. á., & Buiter, S. (2012). Geodynamic models of terrane accretion: Testing the fate of island arcs, oceanic plateaus, and continental fragments in subduction zones. *Journal of Geophysical Research: Solid Earth*, *117*(B8).

van Zelst, I., Crameri, F., Pusok, A. E., Glerum, A., Dannberg, J., & Thieulot, C. (2021). 101 Geodynamic modelling: How to design, carry out, and interpret numerical studies. *Solid Earth Discussions*, 1–80.

Varga, M. D. L., Schaaf, A., & Wellmann, F. (2019). GemPy 1.0: open-source stochastic geological modeling and inversion. *Geoscientific Model Development*, *12*(1), 1–32.

Wellmann, F., & Caumon, G. (2018). 3-D Structural geological models: Concepts, methods, and uncertainties. In *Advances in geophysics* (Vol. 59, pp. 1–121). Elsevier.

Wijns, C., Boschetti, F., & Moresi, L. (2003). Inverse modelling in geology by interactive evolutionary computation. *Journal of Structural Geology*, *25*(10), 1615–1621.

## Supporting Information References

## References

Baumann, T. S., Kaus, B., & Popov, A. A. (2018). Deformation and stresses related to the gorleben salt structure: insights from 3d numerical models. *Mechanical Behavior of Salt, Saltmech IX*, 15–27.

Crameri, F., Schmeling, H., Golabek, G. J., Duretz, T., Orendt, R., Buiter, S., . . . Tackley, P. (2012). A comparison of numerical surface topography calculations in geodynamic modelling: an evaluation of the 'sticky air'method. *Geophysical Journal International*, *189*(1), 38–54.

Drucker, D. C., & Prager, W. (1952). Soil mechanics and plastic analysis or limit design. *Quarterly of applied mathematics*, *10*(2), 157–165.

Harlow, F. H., & Welch, J. E. (1965). Numerical calculation of time-dependent viscous incompressible flow of fluid with free surface. *The physics of fluids*, *8*(12), 2182–2189.

Ingraham, M. D., Broome, S. T., Bauer, S. J., Barrow, P. C., & Flint, G. M. (2015, June). Behavior of salt from the bayou choctaw salt dome. In *49th us rock mechanics/geomechanics symposium.*

Kaus, B. J. P., Mühlhaus, H., & May, D. A. (2010). A stabilization algorithm for geodynamic numerical simulations with a free surface. *Physics of the Earth and Planetary Interiors*, *181*(1-2), 12–20.

Martinod, J., Husson, L., Roperch, P., Guillaume, B., & Espurt, N. (2010). Horizontal subduction zones, convergence velocity and the building of the Andes. *Earth and Planetary Science Letters*, *299*(3-4), 299–309.

Zong, J., Stewart, R. R., Dyaur, N., & Myers, M. T. (2017). Elastic properties of rock salt: Laboratory measurements and gulf of mexico well-log analysis. *Geophysics*, *82*(5), D303–D317.

GEOCHEMISTRY, GEOPHYSICS, GEOSYSTEMS

# Supporting Information for "Geodynamic Modeling with Uncertain Initial Geometries"

A. Spang [1], T. S. Baumann [1], B. J. P. Kaus [1,2]

[1]Johannes Gutenberg University, Institute of Geosciences, Johann-Joachim-Becher-Weg 21, 55128 Mainz, Germany

[2]TeMaS, Terrestrial Magmatic Systems Research Center, temas.uni-mainz.de

**Contents of this file:**



---

Corresponding author: A. Spang, Department of Geosciences, Johannes Gutenberg University, Johann-Joachim-Becher-Weg 21, 55128 Mainz, Germany. (arspang@uni-mainz.de)

## Introduction

This file contains supplementary texts about methodology (S1: General workflow, S2: Additional Options, S3: Model Details), results (S4: Asymmetry) and a simple inversion example for the subduction application (S5: Inverting for Initial Angle). Furthermore, it contains the supplementary Figures S1 to S5 associated with methodology, Figures S6 to S9 associated with Application I: Salt, Figure S10 associated with Application II: Subduction and Figure S11 associated with text S5. Finally, supplementary tables S1 and S2 containing the material parameters used and table S3 containing scaling parameters used in Application I: Salt.

**Text S1: General workflow**

This text outlines the general workflow of how our tool can be used for a geodynamic study. It contains 7 steps (illustrated in Figure S1), of which the last 4 may repeat if an inversion is to be performed. Steps 1-4, 6 and 7 can be completed on any modern computer or laptop that has access to Inkscape, Matlab and Paraview (for visualization only). Step 5 requires LaMEM and more computing power. Single 2D simulations can be performed on regular machines but for 3D or a large number of 2D simulations, a computing cluster is necessary.

(i) Draw the reference geometry in Inkscape. This includes all units like the background lithosphere, mantle and anomalous bodies like salt and magma bodies or subducting plates. Instructions can be found at: https://bitbucket.org/geomio/geomio/wiki/Home. This results in an .svg file.

(ii) Use the basic functionality of geomIO to read the .svg file and create the reference geometry. This results in a .vtk file for each unit. The different units can be visualized directly in Matlab. Alternatively, the .vtk files can be opened in Paraview.

(iii) Choose the unit that should be varied and the control polygons. Prepare and load in scaling parameters for each variation or use the build-in options to generate them.

(iv) Use the new functionality of geomIO and the options selected in step (iii) to create an ensemble of setups. Figure S2 shows examples of how this can be accomplished. For a more detailed description of all available options visit https://bitbucket.org/geomio/geomio/wiki/VaryGeomTutorial.md.

(v) Use LaMEM to run forward models with each of the setups generated in step (iv).

(vi) Use any software to post-process the results from LaMEM (e.g. compute a misfit to observations, analyze result dependencies on input parameters). LaMEM output is in .vtk format, so it can be directly visualized in Paraview, or read and reformatted in Python or Julia.

(vii) Optional: Select new scaling parameters and return to step (iv). New scaling parameters can be the result of an optimization algorithm (e.g., neighborhood algorithm (Sambridge, 1999), NAplus (Baumann et al., 2014)).

To reproduce the results (including Figures) of this study, visit our repository on zenodo (https://doi.org/10.5281/zenodo.6538270). It contains the versions of geomIO and LaMEM that were utilized as well as detailed step-by-step instructions of how to reproduce our results. As LaMEM requires more computing power, we also included the post-processed output in the repository.

## Text S2: Additional Options

### Text S2.1: Absolute Transformation Parameters

One issue of the method described in section 2.1.3 is that the absolute change in coordinates of polygon nodes is determined by the size of the polygon. In Figure S3b, the central polygon (lowermost control polygon) is elongated by 0.5 units in y-direction while the lowermost polygon is only elongated by 0.015 units. If this effect is not desired, we offer a second transformation algorithm which works with absolute transformation parameters ($dx$ and $dy$). $dx$ and $dy$ are the maximum transformations per direction and they are scaled for every node on the polygon, depending on the node's position:

$$\begin{pmatrix}\vec{x}_{new} & \vec{y}_{new}\end{pmatrix} = \begin{pmatrix}\vec{x} & \vec{y}\end{pmatrix} + \begin{pmatrix}\frac{\vec{x}'}{|\overrightarrow{xy}|} & \frac{\vec{y}'}{|\overrightarrow{xy}|}\end{pmatrix} * \begin{pmatrix}dx & 0 \\ 0 & dy\end{pmatrix} \tag{S1}$$

$$|\overrightarrow{xy}|_n = \sqrt{{x'_n}^2 + {y'_n}^2} \tag{S2}$$

The fraction in equation S1 corresponds to element-wise division. The lower half of the body in Figure S3c was changed with absolute transformation parameters. While the central polygon (lowermost control polygon) is identical to the one in Figure S3b, all polygons below are wider, most notably the lowest one. Figure S4a shows how the different methods affect the lowermost polygon. The approach of absolute transformation is limited when it comes to shrinking parts of the body which have very small polygons.

**Text S2.2: Coordinate rotation**

The body might have a preferred orientation which is not aligned with either the x- or the y-direction, so scaling it in a different direction might be desirable. To do that, we include the option to rotate the coordinate system such that the orientation, in which transformation is preferred, aligns with one of the axes. This is done by defining the rotation matrix

$$Q = \begin{pmatrix} cos(\theta) & sin(\theta) \\ -sin(\theta) & cos(\theta) \end{pmatrix} \tag{S3}$$

where $\theta$ represents the preferred direction of transformation and rotates the coordinate system clockwise. To apply it, equation 3 has to be modified to:

$$\begin{pmatrix} \vec{x}_{i,new} & \vec{y}_{i,new} \end{pmatrix} = \begin{pmatrix} \vec{x_i}' & \vec{y_i}' \end{pmatrix} * Q * \begin{pmatrix} Sx_1 & 0 \\ 0 & Sy_1 \end{pmatrix} * Q^T + \begin{pmatrix} x_{i_c} & y_{i_c} \\ ... & \\ x_{i_c} & y_{i_c} \end{pmatrix} \tag{S4}$$

Figure S4b shows an example case where a polygon is elongated in NNE-SSW direction, so without rotating the coordinate system it would not be possible to only transform the polygon along its longest axis. However, by rotating the y-axis to align with the orientation, then applying the scaling and rotating it back, we can do that. Figure S4c shows that more complex shapes can be handled in the same way.

**Text S3.1: LaMEM**

For our models, we utilize the thermomechanical finite differences code LaMEM (Kaus et al., 2016). It solves for the conservation of momentum, mass and energy (eq. S5-S7), using a staggered grid in combination with a marker-in-cell approach (Harlow & Welch, 1965).

$$\frac{\partial \tau_{ij}}{\partial x_j} - \frac{\partial p}{\partial x_i} + \rho g_i = 0 \tag{S5}$$

$$\frac{1}{K}\frac{Dp}{Dt} - \alpha\frac{DT}{Dt} + \frac{\partial v_i}{\partial x_i} = 0 \tag{S6}$$

$$\rho C_p \frac{DT}{Dt} = \frac{\partial}{\partial x_i}\left(\lambda \frac{\partial T}{\partial x_i}\right) \tag{S7}$$

$\tau_{ij}$ is the Cauchy stress deviator, $x_i(i = 1, 2, 3)$ denotes the Cartesian coordinates, $p$ is pressure (positive in compression), $\rho$ density, $g_i$ gravitational acceleration, $K$ the bulk modulus, $\alpha$ the thermal expansion coefficient, $T$ the temperature, $v_i$ the velocity vector, $C_p$ the specific heat capacity, $\lambda$ the thermal conductivity and D/Dt is the material time derivative.

The rocks are characterized by a visco-elasto-plastic rheology where the strain rate is the sum of the elastic, viscous and plastic components:

$$\dot{\epsilon}_{ij} = \dot{\epsilon}_{ij}^{el} + \dot{\epsilon}_{ij}^{vi} + \dot{\epsilon}_{ij}^{pl} \tag{S8}$$

$\dot{\epsilon}_{ij}$ denotes the total deviatoric strain rate tensor, while $\dot{\epsilon}_{ij}^{el}$, $\dot{\epsilon}_{ij}^{vi}$ and $\dot{\epsilon}_{ij}^{pl}$ represent the elastic, viscous and plastic strain rate components. For a detailed discussion of this equation and all of its components, the reader is referred to Kaus et al. (2016). Here we will focus on the material parameters which impact the 3 components.

The elastic component depends on the shear modulus $G$:

$$\dot{\epsilon}_{ij}^{el} = \frac{1}{2G}\frac{D\tau_{ij}}{Dt}, \tag{S9}$$

where $D\tau_{ij}/Dt$ is the objective derivative of the stress tensor.

The viscous component depends on the viscosity $\eta$:

$$\dot{\epsilon}_{ij}^{vi} = \frac{\tau_{ij}}{2\eta} \tag{S10}$$

$\eta$ is either a constant (see tables S1 and S2) or follows the stress- and temperature-dependent powerlaw relationship of dislocation creep:

$$\eta = \frac{1}{2}(B_n)^{-\frac{1}{n}}(\dot{\epsilon}_{II})^{\frac{1}{n}-1}\exp\left(\frac{E_n + pV_n}{nRT}\right), \tag{S11}$$

where $B_n$ is the creep constant, $\dot{\epsilon}_{II}$ the square root of the second invariant of the strain rate ($\dot{\epsilon}_{II} = (\frac{1}{2}\dot{\epsilon}_{ij}\dot{\epsilon}_{ij})^{1/2}$), $E_n$ the activation energy, $p$ the pressure, $V_n$ the activation volume, $n$ the powerlaw exponent, $R$ the universal gas constant and $T$ the temperature.

The plastic component is governed by the Drucker-Prager failure criterion (Drucker & Prager, 1952):

$$\tau_{II} \leq \sin(\phi)p + \cos(\phi)c_0 \tag{S12}$$

where $\tau_{II}$ is the square root of the second invariant of the stress tensor ($\tau_{II} = (\frac{1}{2}\tau_{ij}\tau_{ij})^{1/2}$), $\phi$ is the friction angle, $p$ the pressure and $c_0$ the cohesion. As long as $\tau_{II}$ does not exceed the failure criterion, the stress is accommodated by visco-elastic deformation.

**Text S3.2: Model Details Application I: Salt**

We model a homogeneous slice of crust that is 20 km wide and deep and hosts a 3.5 km thick salt bed from which the diapir rises. Along the boundaries of the model, we employ free slip conditions (velocities normal to boundaries equal zero). At the top of the crust, we use a stabilized (Kaus et al., 2010) stress free internal surface and 5 km thick layer of sticky air (Crameri et al., 2012). We use 128 cells in the horizontal and 256 cells in vertical direction. For simplicity, we use linear viscosities $\eta$ for all materials. Table S1 summarizes the material parameters that we employed. A shear modulus of 15 GPa and a Poisson's ratio of 0.25 correspond to a Young's modulus of 37.5 GPa which is consistent with previous laboratory and modeling studies on salt (Ingraham et al., 2015, June; Zong et al., 2017; Baumann et al., 2018).

**Text S3.3: Model Details Application II: Subduction**

Our subduction model is 2000 km wide and extends from the surface to 660 km depth. We use 512 cells in the horizontal and 256 cells in the vertical direction, yielding resolutions of about 4 and 2.5 km respectively. The 100 km thick continent is made up of 40 km of crust and 60 km of lithospheric mantle. We assign different linear temperature gradients to the continental crust and lithosphere and use a half-space cooling model for the subducting plate that corresponds to a thermal age of 30 Myr. As the plate has already started subducting at the start of our simulations, we add another 1 Myr of temperature diffusion to account for the heating during that initial stage of subduction (Figure S10a). All materials are described by a temperature- and stress-dependent visco-plastic rheology. Table S2 summarizes all material parameters. We use free slip boundary conditions along all model edges and do not prescribe any boundary velocities.

**Text S4: Asymmetry**

The asymmetry was introduced by slightly reducing the curvature of the diapir head on one side (Figure 3, S8). As for the symmetric case, we can see a clear distinction between faults that develop from the center of the diapir head and those that develop from the side of the head (Figure S8a,d). But while central faults still develop to both sides, outside faults now exclusively develop on one side of the diapir (Figure S8c,f). Mirroring the asymmetry leads to a mirrored result. In all cases, outside faults now appear on the side that retained the original curvature.

This suggests that for symmetric cases, the side that develops the dominant fault is influenced by the small difference between how one side of the curved diapir boundary aligns with the grid cells compared to the other side. This is still the case for the central faults at asymmetric diapirs, but towards the outside of the diapir head, the asymmetry is more important for the location of the dominant fault.

**Text S5: Inverting for Initial Angle**

Reconstructions (e.g. Sdrolias & Müller, 2006) show that convergence velocities between plates fluctuate throughout the evolution of subduction zones. These fluctuations are frequently interpreted to be the result of subdcution of ocean plateaus or ridges (e.g. Martinod et al., 2010) but our models show that the convergence rate also fluctuates without any changes in the elevation or density structure of the oceanic plate. Instead the velocity profile seems to be coupled to the initial dip of the subducting slab ($\beta_0$), so given a good understanding of the rheology of the system, a velocity reconstruction could also be used to invert for an initial angle using modeling. To demonstrate the feasibility of this approach, we use a synthetic profile that we generated using $\beta_0 = 72.5°$ (dotted line in Figure S11a). We add normally distributed random noise ($\sigma = 0.5\,\mathrm{cm\,yr^{-1}}$) to the profile to get a synthetic observation in 1 Myr intervals (black circles in Figure S11a). We then run a set of models in 5° intervals (blue in Figure S11b), compute the RMS misfit ($\Phi$) and add models in 1° intervals in areas of low misfit (orange in Figure S11b).

Figure S11b shows that we can find the true $\beta_0$ with only a few forward models. In a real application, there might be more parameters involved in the inversion process but as there is an obvious dependency of the velocity profile on the initial angle, an inversion with more models should still converge to the correct solution.

## References

Baumann, T. S., Kaus, B., & Popov, A. A. (2018). Deformation and stresses related to the gorleben salt structure: insights from 3d numerical models. *Mechanical Behavior of Salt, Saltmech IX*, 15–27.

Baumann, T. S., Kaus, B. J. P., & Popov, A. A. (2014). Constraining effective rheology through parallel joint geodynamic inversion. *Tectonophysics*, *631*, 197–211. doi: https://doi.org/10.1016/j.tecto.2014.04.037

Crameri, F., Schmeling, H., Golabek, G. J., Duretz, T., Orendt, R., Buiter, S., ... Tackley, P. (2012). A comparison of numerical surface topography calculations in geodynamic modelling: an evaluation of the 'sticky air'method. *Geophysical Journal International*, *189*(1), 38–54.

Drucker, D. C., & Prager, W. (1952). Soil mechanics and plastic analysis or limit design. *Quarterly of applied mathematics*, *10*(2), 157–165.

Harlow, F. H., & Welch, J. E. (1965). Numerical calculation of time-dependent viscous incompressible flow of fluid with free surface. *The physics of fluids*, *8*(12), 2182–2189.

Ingraham, M. D., Broome, S. T., Bauer, S. J., Barrow, P. C., & Flint, G. M. (2015, June). Behavior of salt from the bayou choctaw salt dome. In *49th US Rock Mechanics/Geomechanics Symposium.*

Kaus, B. J. P., Mühlhaus, H., & May, D. A. (2010). A stabilization algorithm for geodynamic numerical simulations with a free surface. *Physics of the Earth and Planetary Interiors*, *181*(1-2), 12–20.

Kaus, B. J. P., Popov, A. A., Baumann, T., Pusok, A., Bauville, A., Fernandez, N., & Collignon, M. (2016). Forward and inverse modelling of lithospheric deformation on geological timescales. In *Proceedings of NIC Symposium.*

Martinod, J., Husson, L., Roperch, P., Guillaume, B., & Espurt, N. (2010). Horizontal subduction zones, convergence velocity and the building of the Andes. *Earth and Planetary Science Letters*, *299*(3-4), 299–309.

Sambridge, M. (1999). Geophysical inversion with a neighbourhood algorithm-I. Searching a parameter space. *Geophysical Journal International*, *138*(2), 479-494. doi: 10.1046/j.1365-246X.1999.00876.x

Sdrolias, M., & Müller, R. D. (2006). Controls on back-arc basin formation. *Geochemistry, Geophysics, Geosystems*, *7*(4).

Zong, J., Stewart, R. R., Dyaur, N., & Myers, M. T. (2017). Elastic properties of rock salt: Laboratory measurements and gulf of mexico well-log analysis. *Geophysics*, *82*(5), D303–D317.

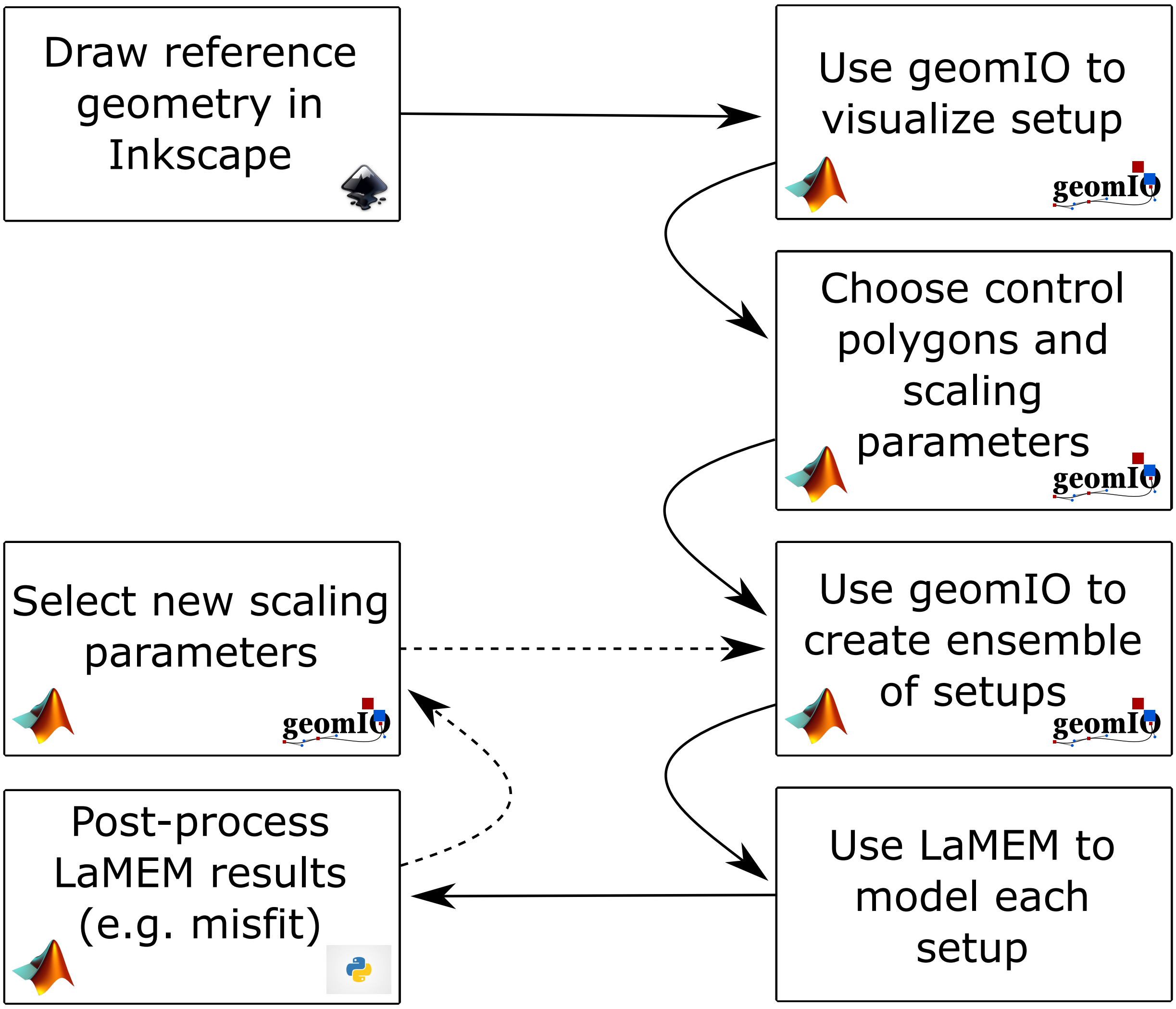


**Figure S1.** General workflow for using geomIO and the new tool presented in this work in combination with LaMEM. The dashed arrows indicate that these steps are optional and are only necessary to minimize misfit or explore additional parameter space. Text S1 describes the procedure in more detail.

(a)

```
% vary geom settings
opt.varyGeom.do             = true;                  % activate geometry vatriation
opt.varyGeom.volume         = 'Diapir';              % name of volume in Inkscape
opt.varyGeom.dim            = '2D_X';                % mode
opt.varyGeom.genType        = 'grid';                % how to generate scaling parameters
opt.varyGeom.Grid.lb        = [0.5; 0.5; 0.5; 0.5];  % lower bound for scaling parameter generation
opt.varyGeom.Grid.ub        = [2.0; 3.0; 2.0; 1.5];  % upper bound for scaling parameter generation
opt.varyGeom.Grid.num       = [2; 2; 2; 2];          % number of samples for each scaling parameter
opt.varyGeom.Grid.Sz        = [0.8; 1.1; 2];         % options for vertical scaling parameter generation
opt.varyGeom.Grid.noise     = 0.3;                   % noise to be added to scaling parameters
opt.varyGeom.stretchType    = 'factor';              % scale by factor or absolute value
opt.varyGeom.SzType         = 'bot';                 % reference level for vertical stretching
opt.varyGeom.CtrlPoly       = [153, 253, 385, 482];  % indices of control polygons
opt.varyGeom.CP_ref         = 'global';              % reference system for control polygons
opt.varyGeom.CP_track       = true;                  % control polygons cahnge depth with vertical scaling
opt.varyGeom.outName        = './SaltExample';       % output name
opt.varyGeom.outNameOffset  = 0;                     % offset numbering of output
opt.varyGeom.writeParaview  = false;                 % write .vtk files
opt.varyGeom.writePolygons  = true;                  % write LaMEM polygons
opt.varyGeom.drawOutlines   = true;                  % draw outline along profile
opt.varyGeom.outlineProf    = [0, 0];                % coordinates of outline profile
```

(b)

```
% vary subduction settings
opt.varySub.do           = true;         % activate subduction variation
opt.varySub.vols         = 'SimpleSlab'; % name of volume in Inkscape
opt.varySub.ref          = 'trench';     % reference system of rotation center coordinates
opt.varySub.xRot         = [0, 120];     % rotation center coordinates
opt.varySub.theta        = [10, -20];    % angles of rotation
opt.varySub.tolZ         = 1;            % tolerance when identifying the plate
opt.varySub.drawOutlines = true;         % draw outline along profile
opt.varySub.outlineProf  = [0, 0];       % coordinates of outline profile

% options to add layers
opt.varySub.addWZ        = true;         % add a weak zone
opt.varySub.d_WZ         = 20;           % thickness of weak zone
opt.varySub.ID_WZ        = 4;            % LaMEM ID
opt.varySub.type_WZ      = 0;            % LaMEM marker type
opt.varySub.d_Lith       = 100;          % thickness of overriding plate

opt.varySub.addCrust     = true;         % add crust
opt.varySub.d_OC         = 10;           % thickness of crust
opt.varySub.ID_OC        = 5;            % LaMEM ID
opt.varySub.type_OC      = 0;            % LaMEM marker type
```

**Figure S2.** Code snippet examples that show the options that are set in geomIO to create the geometry variations. (a) Salt diapir example. (b) Subduction example. Full codes used in this study are available on zenodo (https://doi.org/10.5281/zenodo.6538270).

Figure S3. Illustration of 3-dimensional bodies as sets of 2-dimensional polygons. The three red polygons are the control polygons which are used to transform the body. (a) Sphere with radius 1, represented as 21 polygons. (b) Sphere from S3a after transformation by scaling. (c) Sphere from S3a with the upper half being transformed by scaling and the lower half by absolute transformation parameters. Note how the lower half is wider in S3c than in S3b.

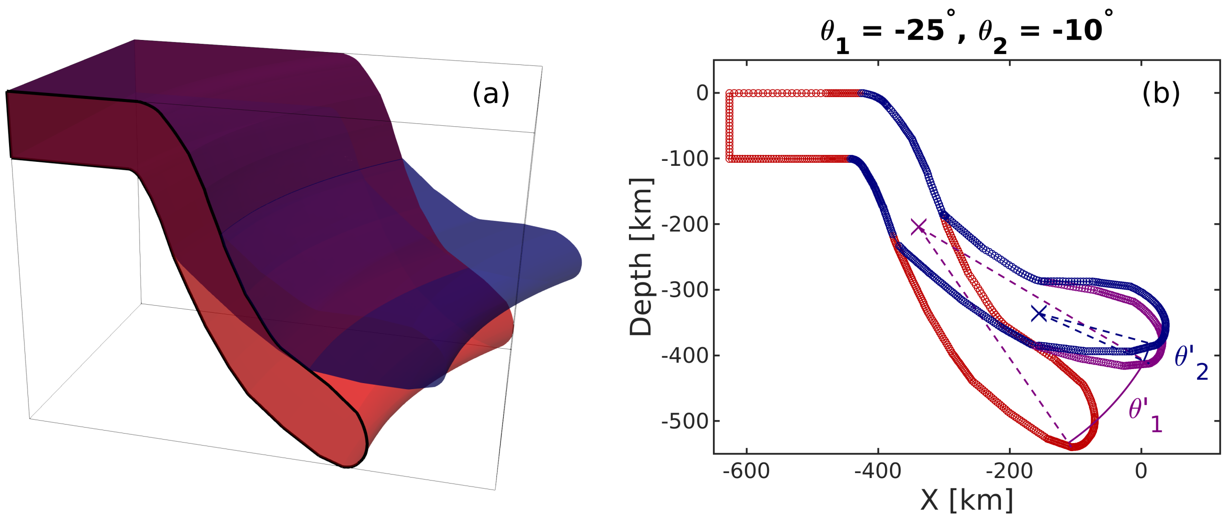


**Figure S5.** (a) 3D Example of a plate, subducting along a curved trench, drawn in geomIO (red) and an automatically generated variation that is bent at two locations in 200 and 320 km depth (crosses in S5b). Black line shows one of the vertical polygons that the 3D volume is represented as inside our algorithm and is identical to the red polygon in S5b. (b) Representation of the plates in S5a as vertical polygons. Red: original, purple: after the first rotation, blue: after both rotations. Crosses show the centers of rotation.

Figure S6. Evolution of plastic strain (i.e. faults) around the synthetic 'true' diapir (blue in Figure 3). (a) Early stage plastic failure along the surface and at the tip of the diapir. (b) First faults start to connect diapir and surface. (c) Faults have connected diapir and surface. Right fault takes up most of the deformation. (d) Right fault takes up all the deformation and left fault is no longer active.